Microwave Imaging via Space-Time Beamforming for Early Detection of Breast Cancer

Essex J. Bond, *Student Member, IEEE*, Xu Li, *Student Member, IEEE*, Susan C. Hagness, *Member, IEEE*, and Barry D. Van Veen, *Fellow, IEEE*

Abstract—A method of microwave imaging via space-time (MIST) beamforming is proposed for detecting early-stage breast cancer. An array of antennas is located near the surface of the breast and an ultrawideband (UWB) signal is transmitted sequentially from each antenna. The received backscattered signals are passed through a space-time beamformer that is designed to image backscattered signal energy as a function of location. The beamformer spatially focuses the backscattered signals to discriminate against clutter and noise while compensating for frequency-dependent propagation effects. As a consequence of the significant dielectric-properties contrast between normal and malignant tissue, localized regions of large backscatter energy levels in the image correspond to malignant tumors. A data-adaptive algorithm for removing artifacts in the received signals due to backscatter from the skin-breast interface is also presented. The effectiveness of these algorithms is demonstrated using a variety of numerical breast phantoms based on anatomically realistic MRI-derived FDTD models of the breast. Very small (2 mm) malignant tumors embedded within the complex fibroglandular structure of the breast are easily detected above the background clutter. The MIST approach is shown to offer significant improvement in performance over previous UWB microwave breast cancer detection techniques based on simpler focusing schemes.

Index Terms—Breast cancer detection, finite-difference time-domain (FDTD), microwave imaging, space-time beamforming, ultrawideband radar.

I. INTRODUCTION

X-RAY mammography remains the preferred method for detecting nonpalpable early-stage breast cancer. Although it provides high-quality images at low radiation doses in the majority of patients, its inherent limitations are well recognized [1]. Most significantly, approximately 15% of all breast cancers present at the time of screening are missed by conventional mammography while nearly three-fourths of all breast lesions that are identified by mammography and biopsied turn out to be benign. The tremendous toll that breast cancer takes, combined with the risks associated with the limited sensitivity and specificity of conventional mammography, motivate the search for alternative technologies for early breast cancer detection. One such alternative is microwave imaging.

The physical basis for microwave detection of breast cancer is the significant contrast in the dielectric properties of normal and malignant breast tissue [2]–[5]. As reviewed in [6], the intrinsic contrast is estimated to be greater than 2:1, whereas for X-rays the contrast is only a few percent. The dielectric properties of malignant tumors show no significant variation with tumor age [7], suggesting that the large contrast exists at the earliest stages of tumor development. The enhanced dielectric properties of breast carcinomas appear to arise in part from increased protein hydration [8]. The contrast is further enhanced by the vascularization of malignant tumors. As a result, malignant tumors have large microwave scattering cross-sections relative to comparably sized heterogeneity in normal breast tissue.

In this paper we propose a method of microwave imaging via space-time (MIST) beamforming for detecting backscattered energy from small malignant breast tumors. This method seeks to identify the presence and location of significant microwave scatterers, that is, malignant lesions, in the breast. The space-time beamformer assumes that each antenna in an array sequentially transmits a low-power ultrawideband (UWB) signal into the breast and records the backscattered signals. The UWB signal may be generated physically as a time-domain impulse or synthetically by using a swept frequency input. The beamformer spatially focuses the backscattered signals to discriminate against clutter caused by the heterogeneity of normal breast tissue and noise while compensating for frequency-dependent propagation effects.

The space-time beamformer achieves this spatial focus by first time shifting the received signals to align the returns from a hypothesized scatterer at a candidate location. The time-aligned signals are passed through a bank of finite-impulse response (FIR) filters, one in each antenna channel, and summed to produce the beamformer output. The weights in the FIR filters are designed using a least squares technique so the beamformer passes the components of the backscattered signal originating from the candidate location with unit gain while compensating for frequency-dependent propagation effects. The beamformer output is time gated to the time interval which would contain the backscattered signal from the candidate location, and then the energy is calculated. If a scattering object, such as a malignant tumor, exists at the candidate location, a relatively large energy results. The beamformer is scanned to different locations by appropriately changing the time shifts, gating, and FIR filter weights. A display of energy as a function of location provides an image of backscattered signal strength.

In contrast to direct matched filtering techniques, MIST beamforming does not assume a specific backscattered signal.

As a result the beamformer maintains robustness with respect to the uncertainty in the shape of the signal that arises from variations in tumor properties, such as size and shape. The beamformer also provides an estimate of the backscattered signal from a specific location that may be further analyzed to gain insight into local tissue properties. Such analysis, e.g., spectral analysis of the backscattered signal, is likely to be useful in tumor characterization. While post-beamforming analysis of backscattered signals is beyond the scope of this paper, the potential of such analysis is strong motivation for a beamforming approach.

Two types of active microwave imaging techniques have been previously proposed for breast cancer detection: tomography [9]–[13] and UWB radar techniques [6], [14]–[16]. The goal of microwave tomography is the recovery of the dielectric-properties profile of the breast from measurements of narrowband microwave signals transmitted through the breast. While promising initial results have been reported [12], the solution of this nonlinear inverse-scattering problem requires challenging and computationally intensive reconstruction algorithms. Also, tomographic techniques generally require a large number of transmitting and receiving antennas to be distributed around the object of interest, which complicates the imaging of smaller breast volumes and breast tissue near the chest wall or in the upper outer quadrant of the breast where nearly half of all lesions occur [17].

In contrast to tomography, UWB radar techniques do not attempt to reconstruct the dielectric-properties profile, but instead seek to identify the presence and location of significant scatterers in the breast. MIST beamforming, which falls under this class of techniques, offers significant improvement over the previously reported techniques of simple time-shifting and summing of backscattered signals to create a synthetically focused signal. A recent computational study [15] illustrates the potential of detecting and imaging millimeter-sized lesions in an anatomically realistic breast model using the simpler approach known as confocal microwave imaging. However, the previous time-shift and summing techniques do not compensate for frequency-dependent propagation effects and have limited ability to discriminate against artifacts and noise.

In addition to the MIST beamforming algorithm, we also present an algorithm for optimally removing artifacts in the received signals due to backscatter from the skin-breast interface. Our approach estimates the skin-breast artifact at each antenna as a filtered combination of the signals at all other antennas. The filter weights are chosen to minimize the residual signal over the initial portion of the received data, which is dominated by the reflection from the skin-breast interface. Our results show that this algorithm effectively eliminates the skin-breast artifact at the expense of an insignificant distortion in the backscattered tumor signal.

The following section of this paper describes our skin-breast artifact removal algorithm. Section III develops our procedure for beamformer design using frequency-dependent propagation models. For ease of presentation we demonstrate our methods in two dimensions (2-D). The design of a 2-D beamformer is illustrated in Section IV. In Section V, we demonstrate the effectiveness of the skin-breast artifact removal and the MIST beam-
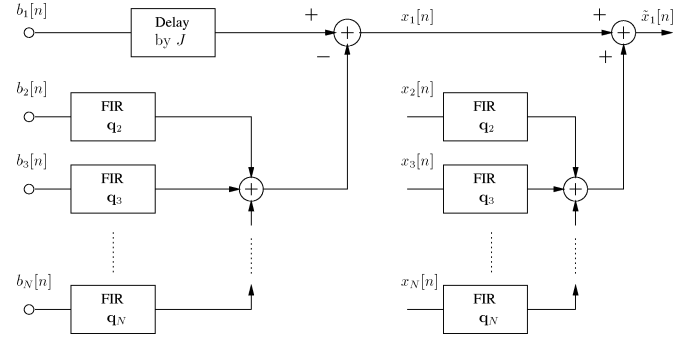

Fig. 1. Block diagram illustrating the algorithm for removing the skin-breast artifact from the backscattered signal received at the first of N antennas.

forming algorithms by applying them to backscattered signals acquired from 2-D computational electromagnetics simulations of an anatomically realistic breast model. We also compare the MIST beamformer performance with the simple time-shift and sum focusing scheme presented in [15] and test the robustness of the MIST approach with respect to hypothesized variations in the breast tissue dielectric properties.

Lower and upper case boldface Roman type is used to denote vector and matrix quantities, respectively. Superscripts T, H, and -1 represent matrix transpose, complex conjugate transpose, and inverse, respectively.

II. SKIN-BREAST ARTIFACT REMOVAL

Consider an array of N antennas and denote the received signal at the ith antenna as $b_i(t)$. Each received signal is converted to a sampled waveform, $b_i[n]$, containing contributions from the skin-breast interface, clutter due to heterogeneity in the breast, backscatter from possible lesions, and noise. The response from the skin-breast interface is orders of magnitude larger than the response from all other contributions and may persist in time beyond the time at which the lesion response occurs. Thus the skin-breast response must be removed prior to performing tumor detection.

The skin-breast artifact in the N channels are similar but not identical due to local variations in skin thickness and breast heterogeneity. If the skin-breast artifact for all channels were identical, it could be removed by subtracting the average of the skin artifact across the N channels from each channel. We have generalized this idea to compensate for channel-to-channel variation by estimating the skin-breast artifact in each channel as a filtered combination of the signal in all other channels as shown in Fig. 1. The filter weights are chosen to minimize the residual signal mean-squared error over that portion of the received data dominated by the reflection from the skin-breast interface.

Without loss of generality, suppose that the skin-breast artifact is to be removed from the first antenna. The skin-breast response at the nth sample in the first channel is estimated from $2J + 1$ successive samples centered on the nth sample in each of the other $N - 1$ channels. Define the $(2J + 1) \times 1$ vector of time samples in the ith antenna channel as

$$\mathbf{b}_i[n] = [b_i[n - J], \cdots, b_i[n], \cdots, b_i[n + J]]^T, \ 2 \leq i \leq N \tag{1}$$

and let $\mathbf{b}_{2N}[n] = [\mathbf{b}_2^T[n], \ldots, \mathbf{b}_N^T[n]]^T$ be the concatenation of data in channels 2 through N. Similarly, let $\mathbf{q}_i$ be the $(2J+1) \times 1$ vector of FIR filter coefficients in the ith channel and $\mathbf{q} = [\mathbf{q}_2^T, \ldots, \mathbf{q}_N^T]^T$ be the concatenation of FIR filter coefficients from channels 2 through N. The optimal filter weight vector $\mathbf{q}$ is chosen to satisfy

$$\mathbf{q} = \arg\min_{\mathbf{q}} \sum_{n=n_0}^{n_0+m-1} \left| b_1[n] - \mathbf{q}^T \mathbf{b}_{2N}[n] \right|^2 \qquad (2)$$

where the time interval $n = n_0$ to $n = n_0 + m - 1$ represents the initial portion of the data record containing skin-breast artifact and no backscattered signals from lesions. The solution to this minimization problem [18] is given by

$$\mathbf{q} = \mathbf{R}^{-1}\mathbf{p} \qquad (3)$$

$$\mathbf{R} = \frac{1}{m} \sum_{n=n_0}^{n_0+m-1} \mathbf{b}_{2N}[n]\mathbf{b}_{2N}^T[n] \qquad (4)$$

$$\mathbf{p} = \frac{1}{m} \sum_{n=n_0}^{n_0+m-1} \mathbf{b}_{2N}[n]b_1[n]. \qquad (5)$$

The fact that there is a high degree of similarity among the skin-breast artifact in all N channels results in the sample covariance matrix $\mathbf{R}$ being ill-conditioned. If $\mathbf{R}$ is ill-conditioned, then the matrix inversion in (3) can result in a solution for $\mathbf{q}$ that has very large norm and thus, amplifies noise. In order to prevent this, we replace $\mathbf{R}$ with the low rank approximation

$$\mathbf{R}_p = \sum_{i=1}^{p} \lambda_i \mathbf{u}_i \mathbf{u}_i^T \qquad (6)$$

where λ_i, $1 \le i \le p$, are the p significant eigenvalues and $\mathbf{u}_i$, $1 \le i \le p$, are the corresponding eigenvectors. The filter weight vector is determined by replacing $\mathbf{R}^{-1}$ in (3) with

$$\mathbf{R}_p^{-1} = \sum_{i=1}^{p} \frac{1}{\lambda_i} \mathbf{u}_i \mathbf{u}_i^T. \qquad (7)$$

The skin-breast artifact is then removed from the entire data record of the first channel to create artifact-free data $x_1[n]$ given by

$$x_1[n] = b_1[n] - \mathbf{q}^T \mathbf{b}_{2N}[n]. \qquad (8)$$

This algorithm introduces a small level of distortion in the backscattered signal from the lesion because the tumor response in the other $N-1$ channels is added back in to the first channel. This is explicitly shown by decomposing $b_1[n]$ and $\mathbf{b}_{2N}[n]$ into skin-breast artifacts $s_1[n]$ and $\mathbf{s}_{2N}[n]$ and residuals $d_1[n]$ and $\mathbf{d}_{2N}[n]$, respectively. The values n_0 and m are chosen so that $\mathbf{q}$ is determined from a portion of the data in which the residuals are negligible and thus,

$$s_1[n] - \mathbf{q}^T \mathbf{s}_{2N}[n] \approx 0. \qquad (9)$$
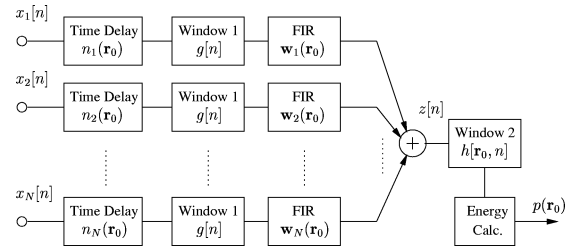

Fig. 2. Block diagram illustrating the MIST beamforming process for location $\mathbf{r}_0$ in the breast.

However, expanding $b_1[n]$ and $\mathbf{b}_{2N}[n]$ in (8) in terms of skin-breast artifacts and residuals gives

$$x_1[n] = s_1[n] - \mathbf{q}^T \mathbf{s}_{2N}[n] + d_1[n] - \mathbf{q}^T \mathbf{d}_{2N}[n] \qquad (10)$$

$$\approx d_1[n] - \mathbf{q}^T \mathbf{d}_{2N}[n]. \qquad (11)$$

Thus the residual signal is distorted by $\mathbf{q}^T \mathbf{d}_{2N}[n]$. This term is generally small because $\mathbf{q}$ tends to "average" across the N channels and the signals in $\mathbf{d}_{2N}[n]$ that represent backscatter from the lesion are not aligned in time, thus they do not add in phase. If the residual $\mathbf{d}_{2N}[n]$ were available, one could remove the distortion by filtering $\mathbf{d}_{2N}[n]$ with $\mathbf{q}$ and adding to $x_1[n]$. We may approximate this correction step by using $\mathbf{x}_{2N}[n]$ to approximate $\mathbf{d}_{2N}[n]$ where

$$\mathbf{x}_{2N}[n]$$
$$= [x_2[n-J], \cdots, x_2[n+J], \cdots, x_N[n-J], \cdots, x_N[n+J]]^T \qquad (12)$$

is the vector containing the data from the other $N-1$ channels after the skin-breast artifact has been removed from each of them. That is, we reduce the distortion in $x_1[n]$ by replacing $x_1[n]$ with $\tilde{x}_1[n]$ where

$$\tilde{x}_1[n] = x_1[n] + \mathbf{q}^T \mathbf{x}_{2N}[n]. \qquad (13)$$

III. MIST BEAMFORMING

The image of backscattered energy as a function of scan location $\mathbf{r}$ is obtained by applying a space-time beamformer designed for each scan location to the backscattered signals measured at each antenna. The space-time beamformer for each scan location forms a weighted combination of time-delayed versions of the backscattered signals as shown in Fig. 2. In this section, we consider the design of a space-time beamformer for a specific scan location $\mathbf{r}_0$. Our goal is to design the beamformer to pass backscattered signals from $\mathbf{r}_0$ with unit gain while attenuating signals from other locations [19].

For design purposes, we assume that the received signal in the ith channel only contains the backscatter due to a lesion at location $\mathbf{r}_0$. Let this signal be denoted by $x_i[n]$ and its Fourier transform denoted by

$$X_i(\omega) = I(\omega)S_{ii}(\mathbf{r}_0, \omega), \quad 1 \le i \le N \qquad (14)$$

where $I(\omega)$ is the Fourier transform of the transmitted pulse $i(t)$ and $S_{ii}(\mathbf{r}_0, \omega)$ is an analytical model of the monostatic frequency response associated with propagation through breast tissue from the ith antenna to the scatterer located at $\mathbf{r}_0$ and back. This signal is then delayed by an integer number of samples $n_i(\mathbf{r}_0) = n_a - \tau_i(\mathbf{r}_0)$ so that the signals in each channel are approximately aligned in time. Here $\tau_i(\mathbf{r}_0)$ denotes the roundtrip propagation delay for location $\mathbf{r}_0$ in the ith channel, computed by dividing the roundtrip path length by the average speed of propagation and rounding to the nearest sample; n_a is the reference time to which all received signals are aligned. We choose n_a as the worst case delay over all channels and locations, that is,

$$n_a \geq \text{round}(\max_{i,\mathbf{r}_0} \tau_i(\mathbf{r}_0)). \tag{15}$$

The time aligned signals are windowed before the filtering stage to remove interference and clutter that is present prior to time n_a using the window function

$$g[n] = \begin{cases} 1, & n \geq n_a \\ 0, & \text{otherwise.} \end{cases} \tag{16}$$

The purpose of the FIR filters is to equalize path length dependent dispersion and attenuation, interpolate any fractional time delays remaining in the backscattered lesion responses after coarse time alignment, and bandpass filter the signal. The FIR filter in the ith channel has coefficients represented by the $L \times 1$ vector $\mathbf{w}_i = \begin{bmatrix} w_{i0}, w_{i1}, \cdots, w_{i(L-1)} \end{bmatrix}^T$. The filter length, L, is chosen empirically to balance performance and complexity. The frequency response of each filter is written as

$$W_i(\omega) = \sum_{\ell=0}^{L-1} w_{i\ell} e^{-j\omega\ell T_s} = \mathbf{w}_i^T \mathbf{d}(\omega) \tag{17}$$

where $\mathbf{d}(\omega) = \begin{bmatrix} 1, e^{-j\omega T_s}, \cdots, e^{-j\omega(L-1)T_s} \end{bmatrix}^T$ and T_s is the sampling interval. In order to pass signals from a location $\mathbf{r}_0$ with unit gain and a linear phase shift, we require

$$\sum_{i=1}^{N} S_{ii}(\mathbf{r}_0, \omega) e^{-j\omega n_i(\mathbf{r}_0)} W_i(\omega)$$
$$= \sum_{i=1}^{N} \widetilde{S}_{ii}(\mathbf{r}_0, \omega) e^{-j\omega\tau_i(\mathbf{r}_0)} e^{-j\omega n_i(\mathbf{r}_0)} \mathbf{w}_i^T \mathbf{d}(\omega)$$
$$\approx e^{-j\omega(T_s(L-1)/2 + n_a)}. \tag{18}$$

Here $\widetilde{S}_{ii}(\mathbf{r}_0, \omega)$ is the frequency response due to propagation after removing the linear phase shift associated with roundtrip propagation delay, $\tau_i(\mathbf{r}_0)$, and $T_s(L-1)/2$ represents the average time delay introduced by the FIR filter. Combining the phase factors associated with the propagation and the time alignment step according to $n_a = \tau_i(\mathbf{r}_0) + n_i(\mathbf{r}_0)$, we obtain the design constraints on $\mathbf{w}_i$ as

$$\sum_{i=1}^{N} \widetilde{S}_{ii}(\mathbf{r}_0, \omega) \mathbf{w}_i^T \mathbf{d}(\omega) \approx e^{-j\omega T_s(L-1)/2}. \tag{19}$$

If these constraints are satisfied, then the summed output of the FIR filter bank, $z[n]$, has Fourier transform

$$Z(\omega) = I(\omega) e^{-j\omega(T_s(L-1)/2 + n_a)}. \tag{20}$$

The output $z[n]$ is windowed with $h[\mathbf{r}_0, n]$ to eliminate additional clutter, and the energy, $p(\mathbf{r}_0)$, is obtained by taking the sum of the squares of the windowed signal as follows:

$$p(\mathbf{r}_0) = \sum_n |z[n]h[\mathbf{r}_0, n]|^2. \tag{21}$$

The reconstructed image of microwave scattering strength is obtained by scanning $\mathbf{r}_0$ throughout the reconstruction region and plotting beamformer output energy as a function of location.

The following subsections describe details specific to the design of the filter weights $\mathbf{w}_i$ and the design of the window $h[\mathbf{r}_0, n]$.

A. FIR Filter Design

Let the $NL \times 1$ filtering weight vector be $\mathbf{w} = [\mathbf{w}_1^T, \ldots, \mathbf{w}_N^T]^T$. We may rewrite (19) as

$$\mathbf{w}^T \mathbf{d}(\mathbf{r}_0, \omega) \approx e^{-j\omega T_s(L-1)/2} \tag{22}$$

where the $NL \times 1$ vector $\mathbf{d}(\mathbf{r}_0, \omega)$ is given by

$$\mathbf{d}(\mathbf{r}_0, \omega) = \begin{bmatrix} \widetilde{S}_{11}(\mathbf{r}_0, \omega)\mathbf{d}(\omega) \\ \widetilde{S}_{22}(\mathbf{r}_0, \omega)\mathbf{d}(\omega) \\ \vdots \\ \widetilde{S}_{NN}(\mathbf{r}_0, \omega)\mathbf{d}(\omega) \end{bmatrix}. \tag{23}$$

The filters are designed by seeking to approximate (22) on a dense grid of M distinct frequencies across the band $[\omega_\ell, \omega_u]$. To ensure that $\mathbf{w}$ is real-valued, we use positive and negative frequency pairs to construct the grid. Define a matrix containing the $\mathbf{d}(\mathbf{r}_0, \omega)$ at each of the M frequencies as

$$\mathbf{A} = [\mathbf{d}(\mathbf{r}_0, \omega_1), \ldots, \mathbf{d}(\mathbf{r}_0, \omega_M)]. \tag{24}$$

Now (22) is expressed over the band $[\omega_\ell, \omega_u]$ as the system of M equations in NL unknowns

$$\mathbf{w}^T \mathbf{A} \approx \mathbf{f}_d \tag{25}$$

where

$$\mathbf{f}_d = [e^{-j\omega_1 T_s(L-1)/2}, \ldots, e^{-j\omega_M T_s(L-1)/2}]. \tag{26}$$

Thus, the least squares design problem [18], [19] for $\mathbf{w}$ is written as

$$\min_{\mathbf{w}} \left\| \mathbf{w}^T \mathbf{A} - \mathbf{f}_d \right\|_2^2. \tag{27}$$

The minimum-norm solution to this problem is

$$\mathbf{w} = (\mathbf{A}\mathbf{A}^H)^{-1} \mathbf{A} \mathbf{f}_d^H. \tag{28}$$

The solution may have a very large norm if $\mathbf{A}$ is ill-conditioned. A large norm can cause the gain at locations other than $\mathbf{r}_0$ to become large and amplify noise. The robustness of a beamformer

to errors between actual and assumed propagation models is also proportional to the noise gain [20]. Thus, in order to control the noise gain and obtain a robust beamformer, we choose $\mathbf{w}$ to solve the penalized least squares problem

$$\min_{\mathbf{w}} \|\mathbf{w}^T \mathbf{A} - \mathbf{f}_d\|_2^2 + \lambda \|\mathbf{w}\|_2^2 \tag{29}$$

where λ is a constant chosen to trade the norm of $\mathbf{w}$ against the approximation error. The solution to (29) is

$$\mathbf{w} = (\mathbf{A}\mathbf{A}^H + \lambda \mathbf{I})^{-1} \mathbf{A} \mathbf{f}_d^H. \tag{30}$$

B. Window Design

If the beamformer satisfies (19) and the lesion is a point scatterer, then the output $z[n]$ is a time-shifted, attenuated, and sampled version of the transmitted pulse $i(t)$. Both the time shift and pulse shape are known, so in this case the set of samples in $z[n]$ that contain backscattered signal from the tumor is known. If the backscattered signal occupies time points n_h through $n_h + \ell_h$ in $z[n]$, then a natural choice for the window is

$$h[\mathbf{r}_0, n] = \begin{cases} 1, & n_h \leq n \leq n_h + \ell_h \\ 0, & \text{otherwise} \end{cases}. \tag{31}$$

This choice reduces clutter effects by ensuring that the output energy (21) is calculated using only samples of $z[n]$ containing backscattered lesion energy.

In practice, scattering from the tumor is frequency-dependent, so the backscattered signal is a distorted version of the transmitted pulse. These dispersive effects increase the duration of the backscattered signal and complicate window selection. Our preliminary investigations suggest that the extent of the increase in duration is directly proportional to the tumor size. Since we are interested in detecting very small lesions, we have chosen to design $h[\mathbf{r}_0, n]$ assuming a point scatterer model. This gives the largest possible signal-to-clutter ratio (S/C) for small tumors. The S/C for larger tumors is reduced by this choice; however, the backscattered signal from larger tumors is much stronger so a compromised S/C is relatively inconsequential for tumor detection. Note that tapered windows such as a raised cosine or decaying exponential could also be used to preserve signal energy while discriminating against clutter.

IV. DESIGN OF A 2-D SPACE-TIME BEAMFORMER

In order to illustrate the MIST beamforming algorithm presented in Sections II and III, the design of a 2-D space-time beamformer will be discussed. We present the 2-D case only to simplify the presentation; these techniques are directly applicable in three dimensions (3-D). Sections IV-A describes the 2-D propagation model used to design the beamformer, and Sections IV-B describes the design parameters for the 2-D beamformer.

A. 2-D Propagation Model

Frequency-dependent propagation effects are incorporated into the design of the space-time beamformer via a monostatic frequency response, $S_{ii}(\mathbf{r}, \omega)$, which relates the received signal at the ith antenna to the transmitted signal at the ith antenna due to a scatterer located at $\mathbf{r}$. In our 2-D design example, we assume that each antenna is an infinite line source of electric current located at $\mathbf{r}_i$ in a uniform medium of normal breast tissue. We treat the scatterer as a conducting circular cylinder of infinite length and infinitesimal radius compared to the small breast lesions we are interested in detecting. In this case

$$S_{ii}(\mathbf{r}, \omega) = \left[\frac{1}{|\mathbf{r} - \mathbf{r}_i|^{1/2}} e^{-\alpha(\omega)|\mathbf{r} - \mathbf{r}_i|} e^{-j\beta(\omega)|\mathbf{r} - \mathbf{r}_i|} \right]^2 \tag{32}$$

where $\alpha(\omega)$ is the frequency-dependent attenuation factor and $\beta(\omega)$ is the frequency-dependent phase constant. We note that a far-field approximation is inherent in (32). Our investigations have shown that approximating the propagating signal as a uniform cylindrical wave gives results which do not vary significantly from those given by a more accurate propagation model based on Hankel functions. We also assume in (32) that the permittivity and conductivity embedded in $\alpha(\omega)$ and $\beta(\omega)$ are constant, evaluated at the spectral peak of the input signal.

B. 2-D Beamformer Design

In this example, the 2-D beamformer is designed for a 1-D conformal antenna array containing 17 elements spanning 8 cm horizontally along the surface of the breast. The 2-D breast region which the beamformer is designed to scan encompasses a span of 10 cm and a depth of 4 cm. The transmitted pulse is a differentiated Gaussian with a full width at half maximum equal to 110 ps. The spectrum of this pulse has a peak near 6 GHz and significant energy between 1 and 11 GHz. Therefore, the beamformer is designed over the range of frequencies of 1 to 11 GHz assuming a 50 GHz sampling frequency. The number of frequency samples used is $M = 1000$. The length of each FIR filter is $L = 45$. Both M and L are chosen so that (22) is approximately satisfied. The penalty parameter λ in (29) is set to 5. The design location $\mathbf{r}$ is scanned over the breast region using a grid resolution of 1 mm. The post-beamformer window described by (21) is six sampling intervals in length, spanning 120 ps.

Fig. 3 illustrates the ideal spatial discrimination capability of this 2-D beamformer. The beamformer gain, defined as the output power due to an idealized point scatterer in a homogeneous medium, is plotted on a dB scale as a function of scatterer position for three different design locations. Although these patterns will deteriorate in the presence of noise and clutter, they are valuable for illustrating the target performance of the beamformer. Fig. 3(a) shows the gain pattern with a peak at (5.0 cm, 3.1 cm) for the case when the beamformer is designed to pass backscattered signals originating from that location with unit gain. In Fig. 3(b), the design location (5.0 cm, 1.1 cm) is 2.0 cm shallower than that of Fig. 3(a). Fig. 3(c) shows the gain pattern for a design location (8.0 cm, 2.1 cm) that is off-center with respect to the antenna array. These patterns show that the beamformer attenuates scattered signals originating from any location that is greater than 1 cm away from the design location by more than 20 dB.
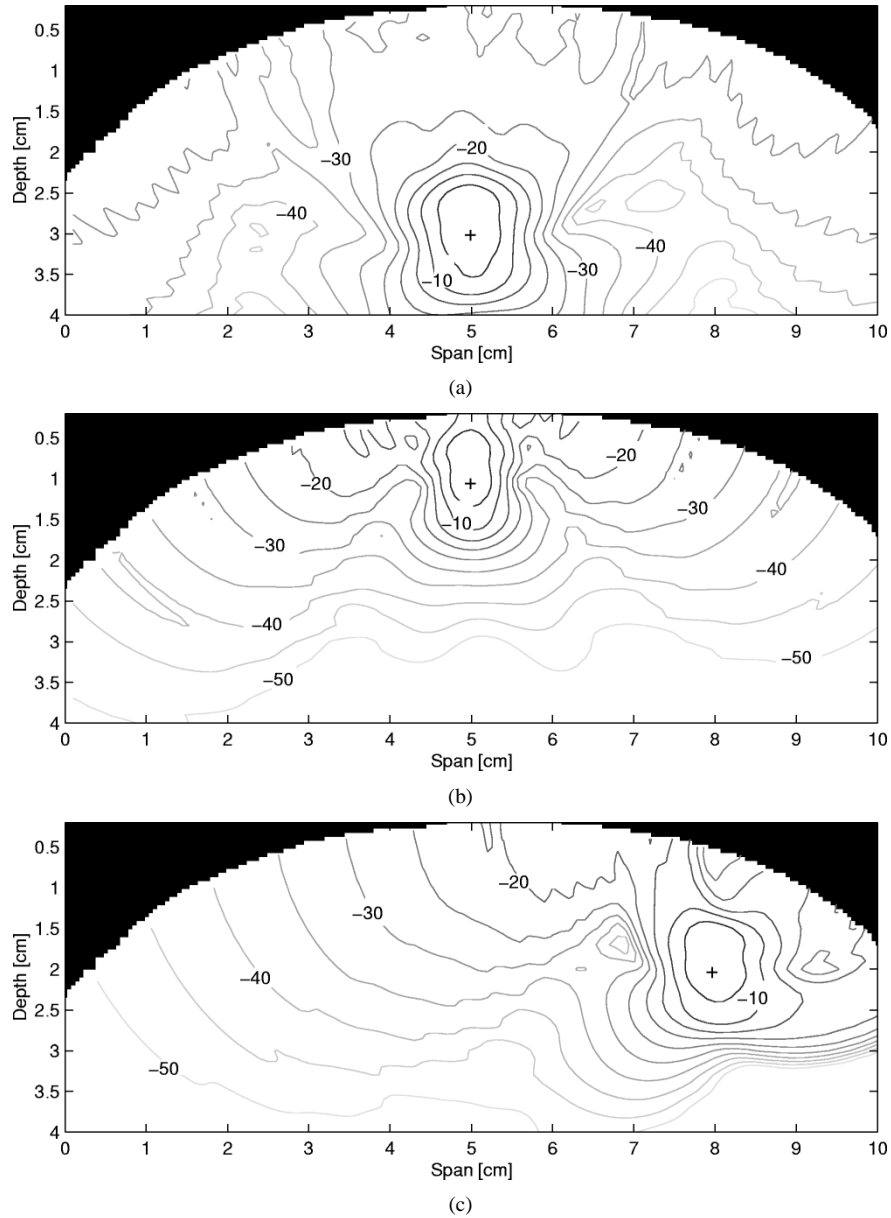
(a)

(b)

(c)

Fig. 3. Beamformer gain as a function of position in a 10 cm × 4 cm plane of the breast for the following design locations: (a) (5.0 cm, 3.1 cm), (b) (5.0 cm, 1.1 cm), (c) (8.0 cm, 2.1 cm). The first and second coordinates in each pair represents span and depth, respectively. In each pattern, the location of the maximum is equal to the design location and is marked by a "+."

V. RESULTS

In this section we demonstrate the effectiveness of the MIST beamforming algorithms by applying them to simulated backscattered signals. First, we review the realistic numerical breast model used to compute a set of backscattered signals. Then, we discuss the results of applying the skin subtraction algorithm to the received backscattered signals. Next, we present and discuss images generated by passing backscattered signals through the space-time beamformer. Lastly, we investigate the robustness of our algorithms using sets of backscattered signals generated from a variety of numerical breast phantoms.

A. Computational Electromagnetics Model for Data Acquisition

Representative backscatter signals are computed using the finite-difference time-domain (FDTD) method [21]. This ap-

proach allows for rapid evaluation of the MIST beamforming algorithms presented in Sections II and III. Our FDTD models simulate the system configuration where a conformal antenna array is placed at the surface of the naturally flattened breast of a patient lying in a supine position. 2-D FDTD models of the breast are derived from high-resolution MRI data sets following the procedure presented in [15] for creating realistic numerical breast phantoms.

Both the dispersive properties and spatial heterogeneity of normal breast tissue are included in our FDTD models. The frequency dependence of the dielectric constant, $\varepsilon_r(\omega)$, and the conductivity, $\sigma(\omega)$, over the band of interest (100 MHz to 20 GHz) can be accurately modeled using single-pole Debye dispersion equations of the following form [15]:

$$\varepsilon_r(\omega) - j\frac{\sigma(\omega)}{\omega\varepsilon_0} = \varepsilon_\infty + \frac{\varepsilon_s - \varepsilon_\infty}{1 + j\omega\tau} - j\frac{\sigma_s}{\omega\varepsilon_0}. \quad (33)$$
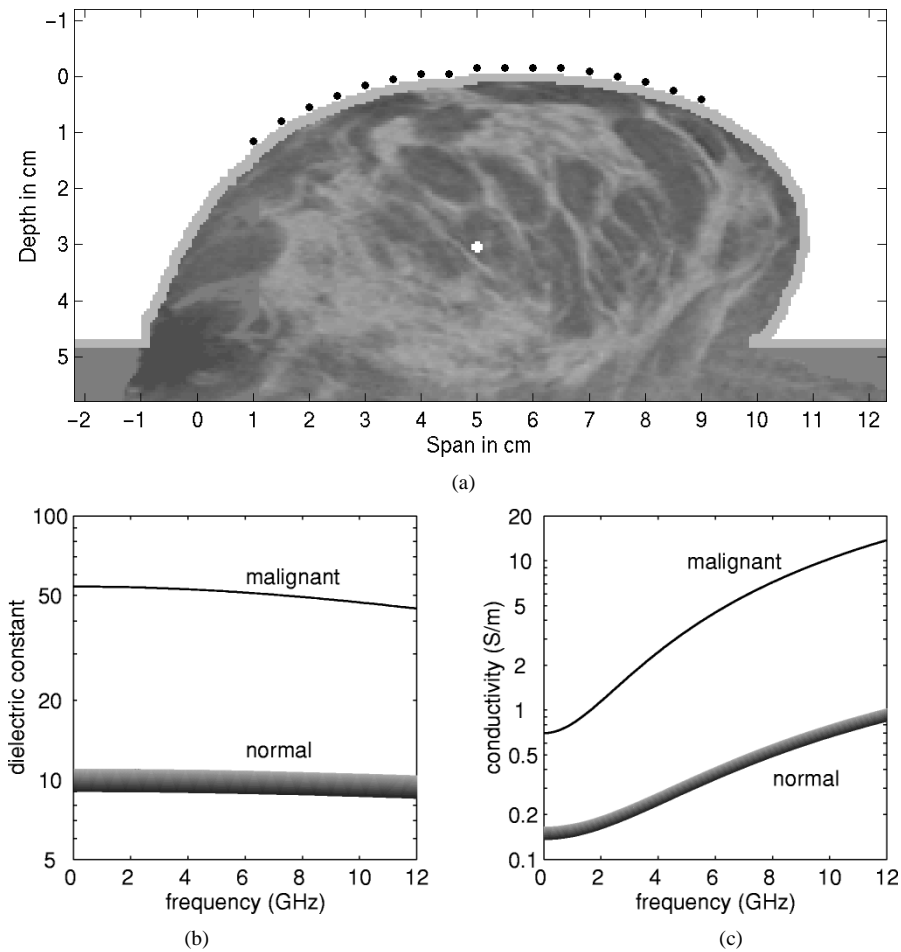
Fig. 4. (a) 2-D MRI-derived FDTD breast model containing a 2-mm-diameter malignant lesion at a depth of 3.1 cm. The 17 black dots along the surface of the breast represent antenna locations. (b) Modeled permittivity and (c) conductivity as a function of frequency for malignant (thin solid curve) and normal (thick shaded curve) breast tissue.

The Debye parameters in (33) are chosen here to fit published data up to 3 GHz for baseline normal ($\varepsilon_s = 10$, $\varepsilon_\infty = 7$, $\sigma_s = 0.15$ S/m, $\tau = 7.0$ ps) and malignant ($\varepsilon_s = 54$, $\varepsilon_\infty = 4$, $\sigma_s = 0.7$ S/m, $\tau = 7.0$ ps) breast tissue. The Debye models are incorporated into the FDTD simulations using an auxiliary differential equation formulation [22]. At any given frequency, the actual dielectric constant and conductivity values for normal breast tissue vary about the nominal dielectric properties by as much as $\pm 10\%$, depending on the local tissue type and density. This variation represents the upper bound on reported breast tissue variability [3], [4]. The high end ($+10\%$) of this range is assigned to denser fibroglandular tissue while the low end (-10%) is assigned to less dense adipose tissue.

Fig. 4(a) shows an example of an MRI-derived FDTD breast model. The grayscale display of the interior breast tissue shows the spatial distribution of dielectric constant and conductivity at a specific frequency (6 GHz). Darker regions represent lower dielectric-property values of adipose tissue while lighter regions represent higher dielectric-property values of fibroglandular tissue. The model includes a 2-mm-thick skin layer ($\varepsilon_r = 36.0$ and $\sigma = 4.0$ S/m at 6 GHz) and a 2-mm-diameter tumor artificially introduced at a depth of 3.1 cm below the surface of the skin. A conformal antenna array consisting of 17 elements modeled as electric-current sources is located on

the surface of the breast along the span-axis between 1.0 cm and 9.0 cm. The location of each antenna is marked by a black dot in Fig. 4(a). The antenna array is backed with a synthetic material matching the dielectric properties of skin. The spatial grid resolution is 0.5 mm, and the time step is $\Delta t = 0.834$ ps ($\sim$ 1200-GHz sampling frequency).

Fig. 4(b) and (c) shows the assumed frequency dependence of the dielectric constant and conductivity of breast tissue in our baseline FDTD model. The thin solid curve represents $\varepsilon_r(\omega)$ and $\sigma(\omega)$ for the malignant lesion. The thick shaded curve illustrates the assumed $\pm 10\%$ variation around the average dielectric properties of normal breast tissue. The grayscale shading of this curve corresponds to that used for normal breast tissue in Fig. 4(a). The Debye model for the average complex permittivity of normal breast tissue yields $\varepsilon_r = 9.8$ and $\sigma = 0.4$ S/m at 6 GHz, the spectral peak of the ultra-wideband input pulse. For malignant breast tissue, the Debye model yields $\varepsilon_r = 50.7$ and $\sigma = 4.8$ S/m at 6 GHz. These values represent a 5:1 contrast in dielectric constant and a 12:1 contrast in conductivity.

A simulated scan involves exciting each antenna-array element individually with a 110-ps differentiated Gaussian pulse and recording the electric-field response at the same antenna element for approximately 2.5 ns. This process is repeated for each element of the array, resulting in 17 received
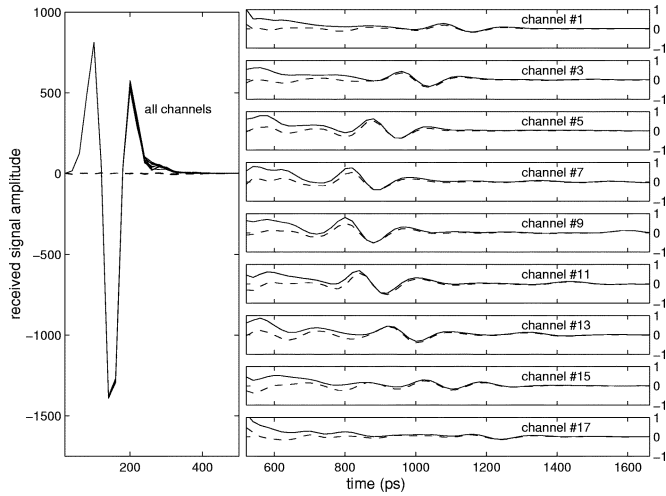
Fig. 5. FDTD computed backscattered signals before applying the skin-breast artifact removal algorithm (solid curves) and after (dashed curves). The left panel shows the early-time response while the right panel shows the late-time response.
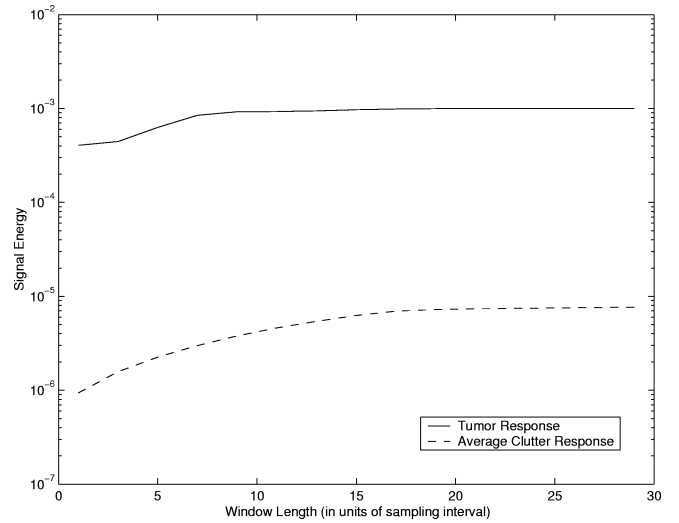

Fig. 6. Signal energy (solid line) and average clutter energy (dotted line) as a function of window length.
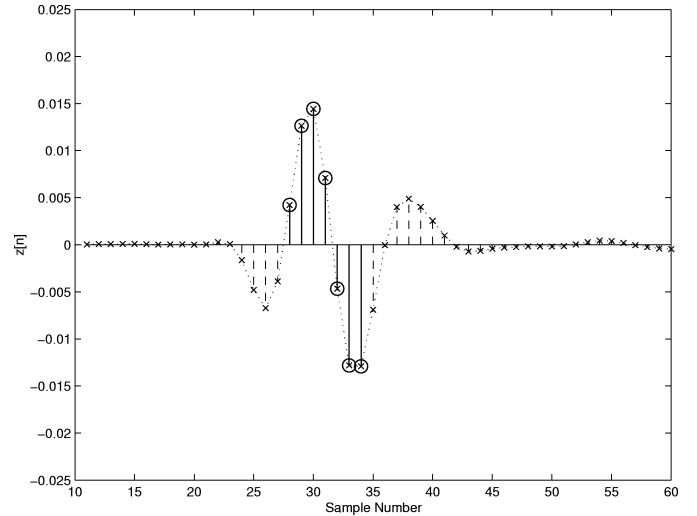

Fig. 7. Output signal when the beamformer is steered to the location of the 2-mm-diameter malignant tumor in the numerical breast phantom of Fig. 4(a). Samples falling within the optimal seven-sample window are signified by a circle surrounding the 'x' of the beamformer output signal.

backscattered signals that contain the scattering contributions from the skin-breast interface (artifact), heterogeneous normal breast tissue (clutter), and the malignant tumor (signal). These sample backscatter signals are representative of those that would be acquired from an actual patient scan and processed using our MIST beamforming algorithms to reconstruct a microwave scattering image of the interior of the breast. In order to prepare these signals for processing, we decimate the signals from a sampling frequency of 1200 GHz to 50 GHz, the sampling frequency assumed in the design of the beamformer described in Section IV-B.

B. Skin-Breast Artifact Removal

The first step in processing the backscatter signals is to remove the skin-breast artifact. Fig. 5 illustrates the effectiveness of the algorithm proposed in Section IV assuming $J = 3$, $p = 15$, and $m = 20$. All 17 received signals, both before and after removing the skin-breast artifact, are plotted in the left (early-time) panel of Fig. 5. A subset of the received signals ($b_i[n]$ and $\tilde{x}_i[n]$ where $i = 1, 3, 5, \ldots, 15, 17$) are plotted in the right (late-time) panel. Prior to applying the skin-breast artifact removal algorithm, the early-time response, shown by the solid curves in the left panel, is dominated by the incident pulse and skin-breast backscatter response. The late-time response, shown by the solid curves in the right panel using an enlarged vertical scale, contains the tumor response and clutter due to heterogeneity in the breast. The incident pulse and skin backscatter response together are three orders of magnitude larger than the strongest tumor response. In this example where each antenna is located at the skin surface, the incident pulse and the response due to the skin-breast interface overlap significantly in time. Thus, the skin artifact removal algorithm is not only eliminating the skin-breast artifact, but also the incident pulse. The left panel shows that the early-time response in the 17 channels are very similar but not identical. The dashed curves represent the processed signals, $\tilde{x}_i[n]$, after applying the skin-breast artifact removal algorithm. The results demonstrate that the early-time

response is almost completely eliminated while the late-time tumor response is preserved in each channel.

C. Space-Time Beamforming Results

The second step in processing the backscatter signals is to apply the beamformer for each scan location in the breast. It is instructive to examine the results at two different stages in this processing step. First, in Figs. 6, 7, and 11, we present results at the next-to-last stage when the window $h[\mathbf{r}_0, n]$ is applied to the output waveform of the beamformer for a specific scan location. Second, in Figs. 8–10 and 12, we present results after the final stage when the beamformer output energy is computed for each scan location and mapped into an image.

Fig. 6 shows typical signal energy and average clutter energy as a function of window length for the case of a 2-mm-diameter tumor centered at (5.0 cm, 3.1 cm). The tumor-response
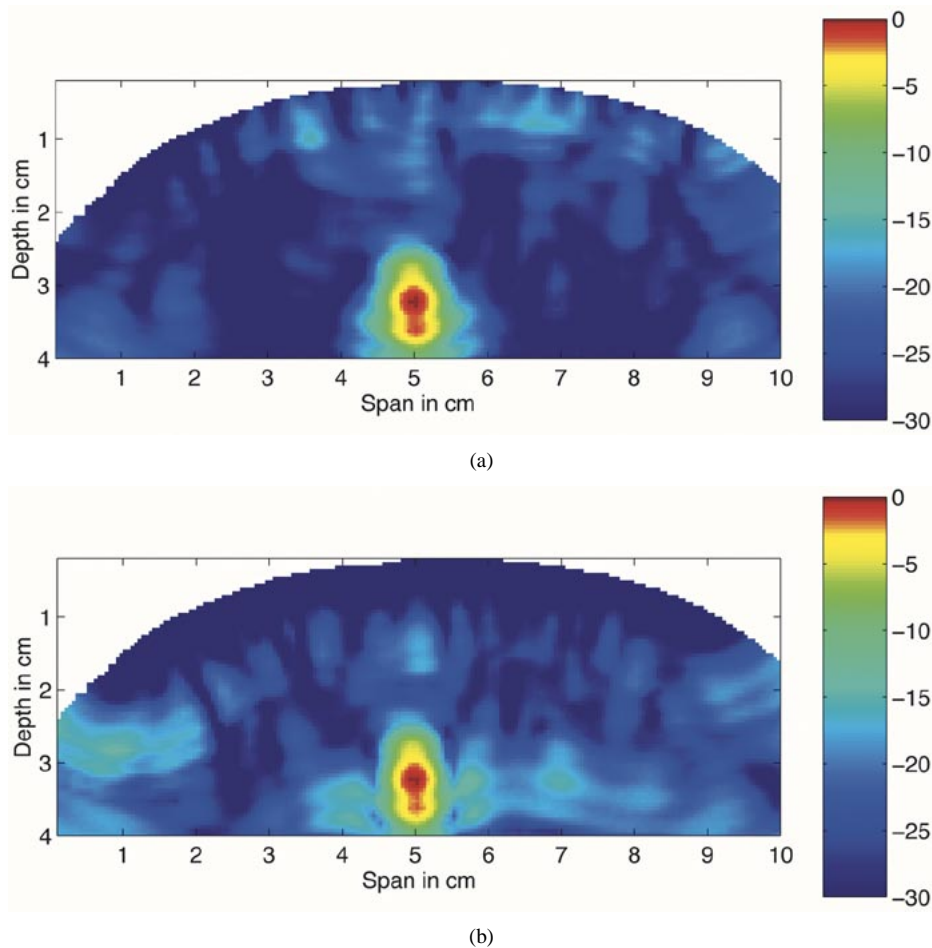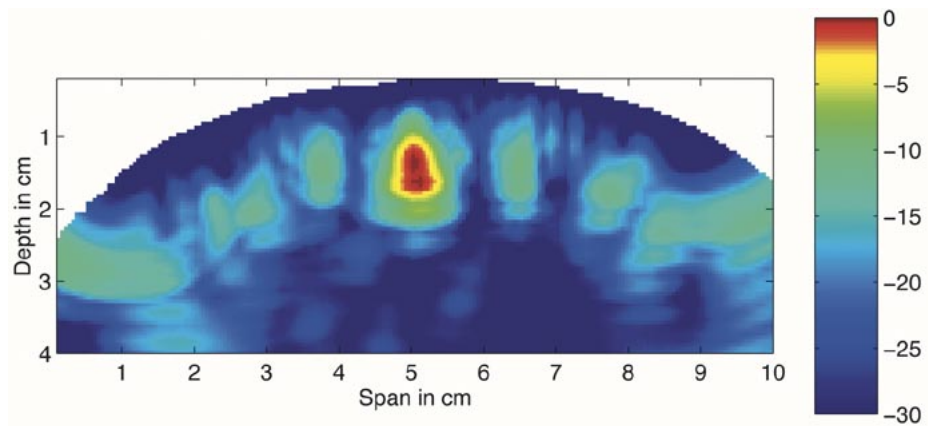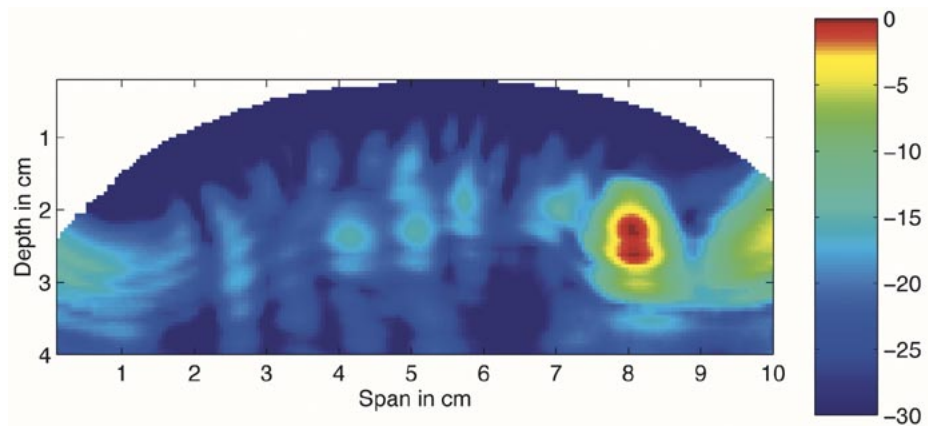
Fig. 8.　Color images showing the backscattered energy on a dB scale for numerical breast phantoms similar to Fig. 4(a) with a 2-mm-diameter malignant tumor centered at (5.0 cm, 3.1 cm). In (a), the skin-breast artifact was removed with an idealized algorithm. In (b), the skin-breast artifact removal algorithm of Section V-B was applied.

data set (solid line) is computed by steering the beamformer to the center location of the tumor, applying windows of varying length to the beamformer output, and calculating output energy. The clutter-response data set (dotted line) is computed by applying the same process to backscatter signals obtained from three tumor-free breast models, repeating for each scan location within the central 6 cm × 2 cm region of each breast, and averaging the results across all three models. These curves illustrate that for small tumors such as the 2-mm-diameter tumor studied here, shorter window lengths yield larger ratios of signal energy to average clutter energy. In fact, Fig. 6 shows that the optimum window length for maximizing this ratio is 6 sampling intervals (120-ps) or a total of seven samples. Fig. 7 shows the position of the seven-sample window relative to the beamformer output signal when the beamformer is steered to the location of the malignant tumor. In this plot, the circled samples fall in the window, and all other samples are outside of the window. Clearly, a larger window would capture more signal energy at this scan location, but that same window would capture more clutter energy when the beamformer is steered elsewhere in the breast. The goal of preserving signal energy while discriminating against clutter suggests this strategy of optimizing S/C rather than signal energy alone.

Fig. 8(a) depicts the scanned beamformer output energy for the breast model of Fig. 4(a) after applying an idealized skin-breast artifact removal algorithm. This idealized algorithm simply subtracts channel-by-channel the exact skin-breast response, that is, the backscatter signal recorded during an FDTD simulation of a tumor-free homogeneous breast model. Obviously, this idealized approach for removing the skin-breast artifact cannot be used in practice. However, in these simulated tests, it serves as a useful benchmark of the best performance possible. The origin of the dominant energy in Fig. 8(a), localized around (5.0 cm, 3.2 cm), is the dielectric-properties contrast between malignant and normal breast tissue. The origin of the low-level energy spatially distributed throughout the image is the heterogeneity of normal breast tissue in the numerical breast phantom. The tumor is clearly detectable as it stands 18 dB above the maximum clutter in the corresponding image for a tumor-free model, a quantity which we term the minimum S/C. Fig. 8(b) depicts the scanned beamformer output energy for the same scenario after the skin-breast artifact removal algorithm described in Section II is applied to the backscattered data. The tumor stands above the maximum background clutter by approximately 17 dB. Comparison of Fig. 8(a) and (b) clearly shows that the skin artifact is removed in Fig. 8(b) at the expense

(c)

(d)

Fig. 8. (*Continued.*) Color images showing the backscattered energy on a dB scale for numerical breast phantoms similar to Fig. 4(a) with a 2-mm-diameter malignant tumor centered at (c) (5.0 cm, 1.1 cm) and (d) (8.0 cm, 2.1 cm). In (c) and (d), the skin-breast artifact removal algorithm of Section V-B was applied.
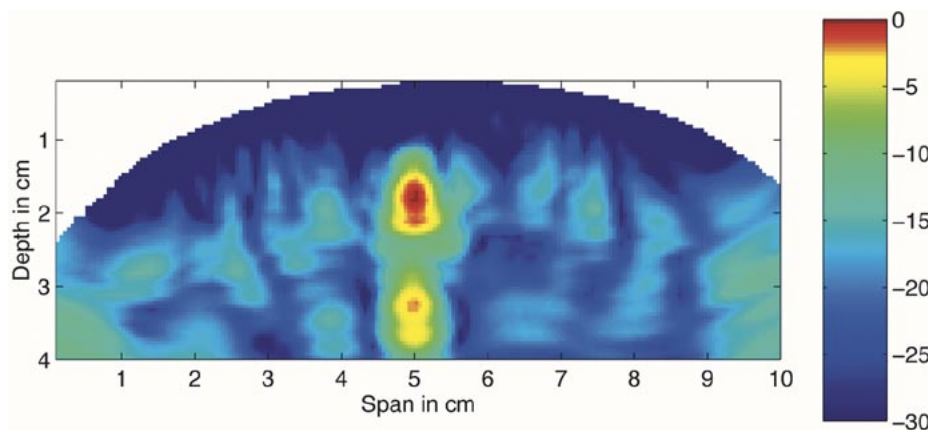

Fig. 9. Color image of backscattered energy plotted on a dB scale for a model similar to that of Fig. 4(a) with two 2-mm-diameter malignant tumors separated by 1.5 cm in the depth direction.

of a small amount of energy from the tumor response spreading throughout the image in the vicinity of the tumor.

Fig. 8(c) and (d) repeat the scenario of Fig. 8(b) for different tumor locations. The image in Fig. 8(c) is based on the backscattered signals computed using a model similar to Fig. 4(a) with the 2-mm-diameter tumor located at a depth of only 1.1 cm. In the model associated with Fig. 8(d), the tumor was located 3.0 cm off the center axis at a depth of 2.1 cm. For the case when the modeled tumor is centered at (5.0 cm, 1.1 cm), the

minimum S/C is 17 dB, and the peak of the tumor response occurs at (5.0 cm, 1.3 cm). When the modeled tumor is centered at (8.0 cm, 2.1 cm), the minimum S/C is 18 dB, and the peak of the tumor response occurs at (8.0 cm, 2.3 cm). In both Fig. 8(c) and (d), energy levels approximately equal to the energy at the peak tumor response location occurs three millimeters deeper than the peak tumor response location.

Fig. 9 depicts the beamformer output energy for two adjacent 2-mm-diameter tumors separated by 1.5 cm with the deeper
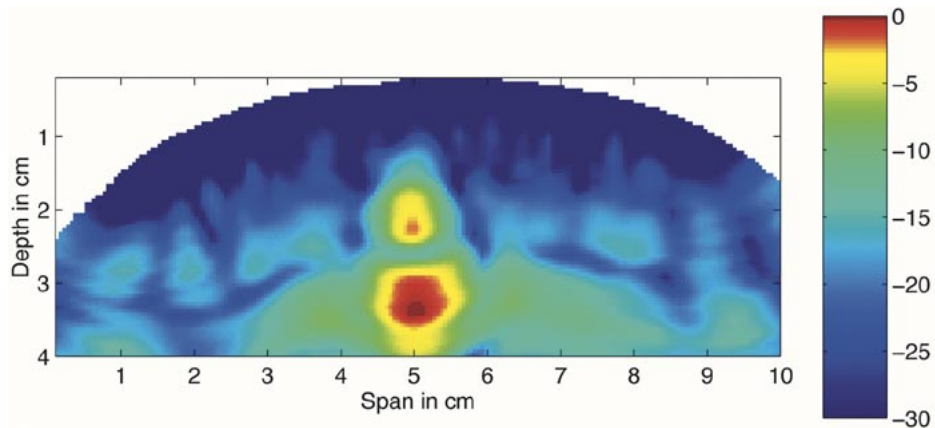
Fig. 10.   Color image of backscattered energy plotted on a dB scale for a model similar to that of Fig. 4(a) with a 6-mm-diameter malignant tumor centered at (5.0 cm, 2.3 cm).

tumor located at a depth of 3.1 cm. Two distinct scattering objects are clearly evident. The tumor response closer to the skin has a minimum S/C of 18 dB while the tumor response farther from the skin has a minimum S/C of 16 dB. This example illustrates the resolving capability of MIST beamforming.

In each of the images of Figs. 8 and 9, the peak of the tumor response occurs 2 to 3 mm deeper than the true center of the tumor. This small localization error is a consequence of assuming that the scatterer is essentially a point-scatterer in the beamformer design and of an inherent bias in the beamforming method toward deeper locations. This bias is due to the requirement that the beamformer compensate for attenuation. These two effects are also responsible for the high energy levels 3 mm deeper than the location of the peak tumor response in Fig. 8(c) and (d) and are clearly illustrated by considering the case of a larger 6-mm-diameter malignant tumor centered at a depth of 2.3 cm. The corresponding image of beamformer output energy depicted in Fig. 10 shows that the peak of the tumor response appears approximately 1 cm deeper than the physical tumor location. Fig. 11(a) depicts the beamformer output signal for scan location (5.0 cm, 2.3 cm), the center of the physical tumor. The samples that fall in the seven-sample window are circled. The finite-sized lossy dielectric scatterer broadens the backscattered signal considerably beyond that predicted by the point-scatterer model, and the window no longer captures the majority of the backscattered signal energy. Fig. 11(b) depicts the beamformer output signal for scan location (5.0 cm, 3.3 cm), the location of the peak of the energy in the image of Fig. 10. While the beamformer eliminates most of the initial backscattered signal present in Fig. 11(a), the late-time portion is preserved, and is actually amplified relative to that in Fig. 11(a) because of the additional gain introduced by the beamformer to compensate for the attenuation associated with a deeper scan location. The seven-sample window captures considerably more energy than that in Fig. 11(a). Note that in spite of the relatively large mismatch between the point-scatterer model and the actual finite-sized tumor, the tumor remains clearly detectable. The S/C is 19 dB, 1 to 2 dB larger than that for the 2 mm tumor.

Finally, we compare the performance of the MIST beamforming method with the simple time-shift and sum focusing scheme presented in [15]. The backscattered signals chosen for this comparison are those computed using the breast model of

(a)

(b)
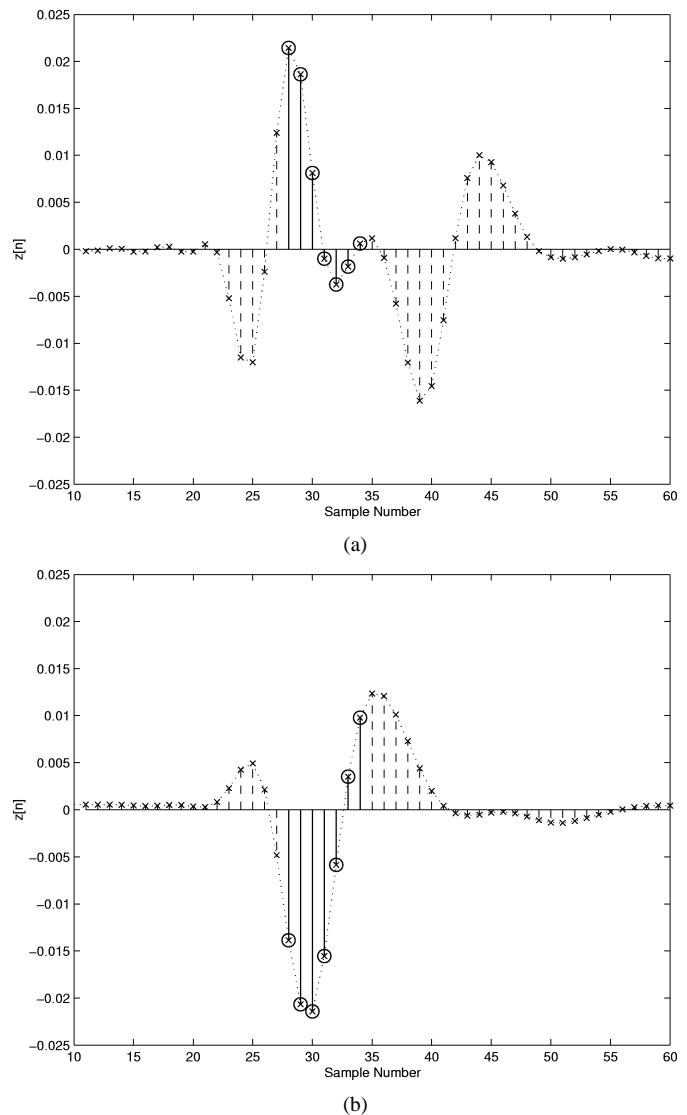
Fig. 11.   Beamformer output signal for scan location (a) (5.0 cm, 2.3 cm), the center of a 6-mm-diameter malignant lesion, and (b) (5.0 cm, 3.3 cm), the location of the peak of the tumor energy in Fig. 10. The 7-sample rectangular window optimized for the case of smaller (2-mm-diameter) lesions is represented by the circled output signal samples.

Fig. 4 and processed with the idealized skin-breast artifact removal algorithm discussed in the context of Fig. 8(a). The min-

TABLE I
RANGE OF DIELECTRIC CONSTANT AND CONDUCTIVITY VALUES AT 6 GHz FOR HETEROGENEOUS NORMAL BREAST TISSUE IN 25 DIFFERENT NUMERICAL BREAST PHANTOMS

Variability	Average Dielectric Properties at 6 GHz				
	$\varepsilon_{r_{\mathrm{avg}}} = 9.8$ $\sigma_{\mathrm{avg}} = 0.4$ S/m	$\varepsilon_{r_{\mathrm{avg}}} = 15.7$ $\sigma_{\mathrm{avg}} = 1.0$ S/m	$\varepsilon_{r_{\mathrm{avg}}} = 21.5$ $\sigma_{\mathrm{avg}} = 1.7$ S/m	$\varepsilon_{r_{\mathrm{avg}}} = 27.3$ $\sigma_{\mathrm{avg}} = 2.3$ S/m	$\varepsilon_{r_{\mathrm{avg}}} = 33.2$ $\sigma_{\mathrm{avg}} = 2.9$ S/m
$\pm 10\%$	$8.82 < \varepsilon_r < 10.8$ $0.36 < \sigma < 0.44$	$14.1 < \varepsilon_r < 17.2$ $0.90 < \sigma < 1.10$	$19.4 < \varepsilon_r < 23.7$ $1.53 < \sigma < 1.87$	$24.6 < \varepsilon_r < 30.0$ $2.07 < \sigma < 2.53$	$29.9 < \varepsilon_r < 36.5$ $2.61 < \sigma < 3.19$
$\pm 20\%$	$7.84 < \varepsilon_r < 11.8$ $0.32 < \sigma < 0.48$	$12.5 < \varepsilon_r < 18.8$ $0.80 < \sigma < 1.20$	$17.2 < \varepsilon_r < 25.8$ $1.36 < \sigma < 2.06$	$21.8 < \varepsilon_r < 32.8$ $1.84 < \sigma < 2.76$	$26.6 < \varepsilon_r < 39.8$ $2.32 < \sigma < 3.48$
$\pm 30\%$	$6.86 < \varepsilon_r < 12.8$ $0.28 < \sigma < 0.52$	$10.9 < \varepsilon_r < 20.4$ $0.70 < \sigma < 1.30$	$15.1 < \varepsilon_r < 27.9$ $1.19 < \sigma < 2.21$	$19.1 < \varepsilon_r < 35.5$ $1.61 < \sigma < 2.99$	$23.2 < \varepsilon_r < 43.2$ $2.03 < \sigma < 3.77$
$\pm 40\%$	$5.88 < \varepsilon_r < 13.7$ $0.24 < \sigma < 0.56$	$9.39 < \varepsilon_r < 21.9$ $0.60 < \sigma < 1.40$	$12.9 < \varepsilon_r < 30.1$ $1.02 < \sigma < 2.38$	$16.4 < \varepsilon_r < 38.2$ $1.38 < \sigma < 3.22$	$19.9 < \varepsilon_r < 46.5$ $1.74 < \sigma < 4.06$
$\pm 50\%$	$4.90 < \varepsilon_r < 14.7$ $0.20 < \sigma < 0.60$	$7.83 < \varepsilon_r < 23.5$ $0.5 < \sigma < 1.50$	$10.8 < \varepsilon_r < 32.3$ $0.85 < \sigma < 2.55$	$13.7 < \varepsilon_r < 41.0$ $1.15 < \sigma < 3.45$	$16.6 < \varepsilon_r < 49.8$ $1.45 < \sigma < 4.35$

TABLE II
S/C AS A FUNCTION OF AVERAGE DIELECTRIC PROPERTIES AND VARIABILITY OF DISPERSIVE NORMAL BREAST TISSUE

Variability	Average Dielectric Properties at 6 GHz				
	$\varepsilon_{r_{\mathrm{avg}}} = 9.8$ $\sigma_{\mathrm{avg}} = 0.4$ S/m	$\varepsilon_{r_{\mathrm{avg}}} = 15.7$ $\sigma_{\mathrm{avg}} = 1.0$ S/m	$\varepsilon_{r_{\mathrm{avg}}} = 21.5$ $\sigma_{\mathrm{avg}} = 1.7$ S/m	$\varepsilon_{r_{\mathrm{avg}}} = 27.3$ $\sigma_{\mathrm{avg}} = 2.3$ S/m	$\varepsilon_{r_{\mathrm{avg}}} = 33.2$ $\sigma_{\mathrm{avg}} = 2.9$ S/m
$\pm 10\%$	18.5 dB	14.6 dB	10.9 dB	4.89 dB	2.82 dB
$\pm 20\%$	14.0 dB	10.7 dB	5.8 dB	1.2 dB	N/A
$\pm 30\%$	11.1 dB	7.9 dB	3.1 dB	N/A	N/A
$\pm 40\%$	9.1 dB	5.9 dB	1.9 dB	N/A	N/A
$\pm 50\%$	7.6 dB	4.4 dB	N/A	N/A	N/A

imum S/C is 9 dB for the method of [15], compared to the 18 dB obtained using MIST beamforming. This significant improvement is a consequence of accounting for frequency-dependent propagation effects and improved discrimination against clutter.

D. Robustness of MIST Beamformer

As previously discussed, the beamformers are designed assuming simple propagation models for a homogeneous breast medium with frequency-independent average dielectric properties. However, the actual backscatter data is acquired either via realistic FDTD simulations as done here or via physical measurements as would be done in an actual patient scan. In either case, the breast tissue is heterogeneous and its dielectric properties are frequency-dependent. These represent significant deviations from the simple propagation physics assumed in the beamformer design. Thus, the successful detection of small lesions in the test cases presented here demonstrates that our MIST beamforming method is inherently robust to deviation between actual propagation effects and assumed propagation models.

Several additional issues related to robustness need to be addressed. In practice, the average density of normal breast tissue and the degree of heterogeneity will vary from patient to patient within a certain margin. Therefore, we investigate the robustness of our MIST beamforming approach with respect to the hypothetical variations in the characteristics of normal breast tissue. We consider scenarios where the average dielectric properties of the normal breast are greater than that suggested by data in the literature as well as scenarios where the variability about the average dielectric properties is greater than that suggested in the literature. Tumor detection under these scenarios is inherently more challenging because of greater signal attenuation, increased clutter, and reduced contrast between malignant and normal tissue.

Table I presents 25 different numerical breast phantoms used throughout this investigation. A 2-mm-diameter tumor is located at (5.0 cm, 2.1 cm) in each phantom. The dispersive properties of normal tissue are incorporated in each numerical breast phantom using (33) and an appropriate set of Debye parameters; however, for ease in presentation of the data, Table I displays single-frequency dielectric property values calculated at the spectral peak of the input pulse. The cell in the upper left corner of the table describes the normal-breast-tissue charac-

TABLE III
LOCATION OF THE DETECTED TUMOR (SPAN IN CM, DEPTH IN CM) AS A FUNCTION OF THE DIELECTRIC PROPERTIES ASSUMED IN THE BEAMFORMER DESIGN AND THE ACTUAL AVERAGE DIELECTRIC PROPERTIES OF THE NUMERICAL BREAST PHANTOM

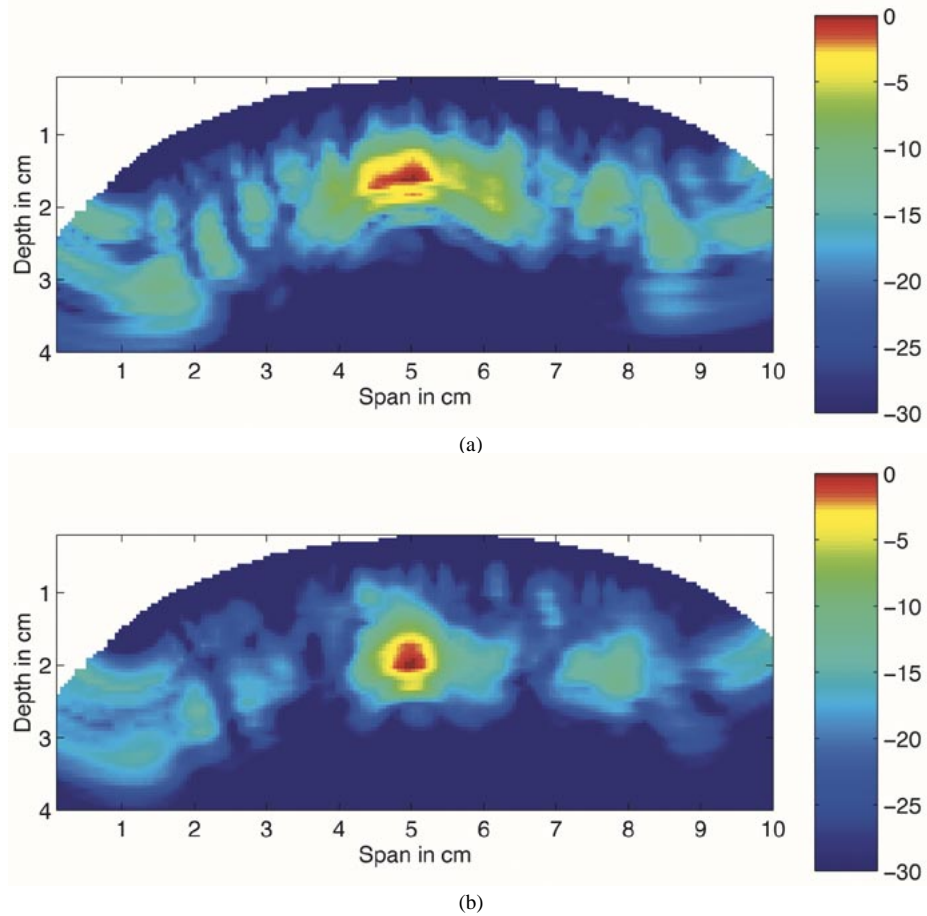| Dielectric properties assumed in beamformer design	Average dielectric properties at 6 GHz of numerical breast phantom				
	$\varepsilon_{r_{avg}} = 9.8$ $\sigma_{avg} = 0.4$ S/m	$\varepsilon_{r_{avg}} = 15.7$ $\sigma_{avg} = 1.0$ S/m	$\varepsilon_{r_{avg}} = 21.5$ $\sigma_{avg} = 1.7$ S/m	$\varepsilon_{r_{avg}} = 27.3$ $\sigma_{avg} = 2.3$ S/m	$\varepsilon_{r_{avg}} = 33.2$ $\sigma_{avg} = 2.9$ S/m
$\varepsilon_r = 9.8$ $\sigma = 0.4$ S/m	(5.0,2.0)	(5.0,2.6)	(5.0,3.0)	(5.1,3.4)	(5.1,3.4)
$\varepsilon_r = 15.7$ $\sigma = 1.0$ S/m	(5.0,1.8)	(5.0,2.3)	(5.0,2.4)	(5.0,2.7)	(5.0,2.7)
$\varepsilon_r = 21.5$ $\sigma = 1.7$ S/m	(5.0,1.6)	(5.0,2.0)	(5.0,2.0)	(5.0,2.3)	(5.0,2.3)
$\varepsilon_r = 27.3$ $\sigma = 2.3$ S/m	(5.0,1.4)	(5.0,1.7)	(5.0,1.9)	(5.0,2.0)	(5.0,2.0)
$\varepsilon_r = 33.2$ $\sigma = 2.9$ S/m	(4.6,1.3)	(5.0,1.5)	(5.0,1.6)	(5.0,1.8)	(5.0,1.8)

(a)

(b)

Fig. 12. Color images of backscattered energy plotted on a dB scale for four numerical breast phantoms each with a 2-mm-diameter malignant tumor centered at (5.0 cm, 2.1 cm). The average dielectric properties of normal breast the first two phantoms are (a) $\varepsilon_{r_{avg}} = 9.8$, $\sigma_{avg} = 0.4$ S/m and (b) $\varepsilon_{r_{avg}} = 15.7$, $\sigma_{avg} = 1.0$ S/m at 6 GHz. The beamformer is designed assuming $\varepsilon_r = 21.5$ and $\sigma = 1.7$ S/m at 6 GHz.

teristics of the baseline numerical breast phantom employed in Section V-C.

Each column in Table I represents one of five different scenarios of normal breast tissue density. The average dielectric properties for the five scenarios are selected as follows. Starting with the baseline normal-tissue and malignant-tissue sets of Debye parameters, we identify six intermediate sets of Debye parameters that are uniformly spaced between the two extremes.
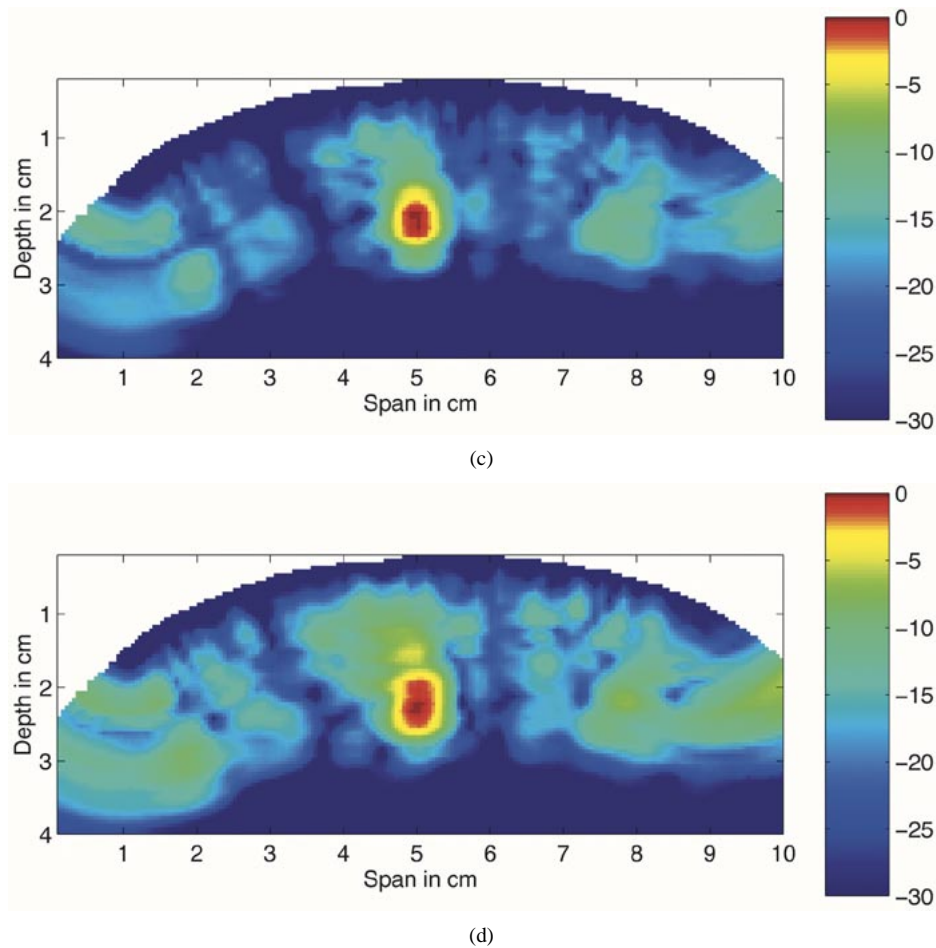
(c)

(d)

Fig. 12. (*Continued.*) The average dielectric properties of normal breast for the last two phantoms are (c) $\varepsilon_{r_{avg}} = 21.5$, $\sigma_{avg} = 1.7$ S/m and (d) $\varepsilon_{r_{avg}} = 27.3$, $\sigma_{avg} = 2.3$ S/m at 6 GHz. The beamformer is designed assuming $\varepsilon_r = 21.5$ and $\sigma = 1.7$ S/m at 6 GHz.

Since the malignant tissue properties remain constant in these investigations, the contrast in the dielectric constant at 6 GHz between malignant and average normal breast tissue decreases from 5.2:1 for the baseline scenario to 3.2:1, 2.4:1, 1.9:1, 1.5:1, 1.3:1, and 1.1:1 for the six intermediate scenarios. The smallest malignant-to-normal contrast in dielectric constant suggested in the literature is approximately 2:1 [12]. Therefore, the first four scenarios are sufficient to span the hypothesized range of normal breast tissue densities. For completeness, we study the first five scenarios.

Each row in Table I represents one of five different scenarios of breast tissue heterogeneity. The upper bound on the variation around the average is increased from ±10% to ±50%. The increased variability further diminishes the contrast between malignant and normal tissue. For example, in the breast phantom described by the last entry in the first column, the contrast between malignant and normal breast tissue decreases from 5.2:1 to 3.4:1 if the tumor is present in the densest region of the breast.

First, we investigate the case where patient-specific (phantom-specific) estimates of the nominal dielectric properties of normal breast tissue are available and are incorporated into the beamformer design process. In this case, the average dielectric properties assumed in the beamformer design stage are matched with the actual average dielectric properties of the numerical breast phantom. Table II shows the S/C obtained for the 25 numerical breast phantoms of Table I. Note that "N/A"

is used for cases when the peak tumor energy is comparable to the background clutter. The S/C decreases as the degree of heterogeneity and/or average dielectric properties are increased, as expected. However, the 2-mm-diameter lesion embedded in heterogeneous normal breast tissue is detectable over a wide range of phantoms, most of which greatly exceed that which is expected in practice. Thus, the results show that our MIST beamforming method is effective even when the average dielectric properties of normal tissue and/or the variability are substantially greater than that reported in the literature.

Second, we investigate the case where patient-specific (phantom-specific) estimates of the nominal dielectric properties of normal breast tissue are not available. In this case, the average dielectric properties assumed in the beamformer design are not matched with the actual average dielectric properties of the numerical breast phantom. For this investigation, the variability is fixed at ±10%, which corresponds to the numerical breast phantoms from the first row of Table I. The constant dielectric constant and conductivity values assumed when designing the beamformer are varied over the same five scenarios as the actual average values. In Table III, we show the location of the peak energy in the resulting image for each combination of actual and assumed average dielectric properties. As expected, the table shows that the tumor is most accurately localized when the actual average dielectric properties are equal to those assumed in the beamformer design. Fig. 12(a)–(d)

show the images of MIST beamformer output energy for the results in the first four columns of the 3rd row of Table III. In all cases, the tumor is still clearly detectable. The primary effect of mismatch between actual and assumed dielectric properties is a location bias. This bias is consistent with the corresponding differences in average speed of propagation.

VI. CONCLUSION

A space-time beamforming method for imaging backscattered microwave energy is proposed and demonstrated for detecting millimeter-sized malignant tumors in the breast. Our results show that this method is exceptionally robust with respect to a number of potential challenges associated with imaging the inherently heterogeneous breast. Due to the enhanced synthetic-focusing capabilities of the MIST beamforming approach, the imaged backscatter from a 2-mm-diameter tumor stands out significantly above the clutter generated by the natural variations in the fibroglandular and adipose composition of the breast. Small lesions can be detected with high sensitivity regardless of location in the breast. The spatial selectivity of MIST beamforming also overcomes the challenge of detecting, localizing, and resolving multiple or multifocal lesions. Small tumors embedded in heterogeneous normal breast tissue are successfully detected in a wide range of numerical breast phantoms, even when the contrast between malignant and normal tissue is significantly reduced due to the presence of denser normal breast tissue. Small tumors are also successfully detected even when a significant mismatch exists between the average normal-breast-tissue dielectric properties assumed in the beamformer design and the actual average dielectric properties of the breast being scanned. Consequently, patient-specific data on the average dielectric properties of normal breast tissue does not appear to be required for detection. The dominant backscatter from the skin-breast interface, which would otherwise overshadow the backscatter from a malignant tumor in the breast, is effectively suppressed by the data-adaptive algorithm designed for removing this artifact. This skin-breast artifact removal algorithm uses only the received backscatter signals and does not require any *a priori* information about the dielectric properties or thickness of the skin.

REFERENCES

[1] *Mammography and Beyond: Developing Techniques for the Early Detection of Breast Cancer*. Washington, D.C.: Institute of Medicine, National Academy Press, 2000.

[2] A. J. Surowiec, S. S. Stuchly, J. R. Barr, and A. Swarup, "Dielectric properties of breast carcinoma and the surrounding tissues," *IEEE Trans. Biomed. Eng.*, vol. 35, pp. 257–263, Apr. 1988.

[3] W. T. Joines, Y. Z. Dhenxing, and R. L. Jirtle, "The measured electrical properties of normal and malignant human tissues from 50 to 900 MHz," *Med. Phys.*, vol. 21, pp. 547–550, Apr. 1994.

[4] S. S. Chaudhary, R. K. Mishra, A. Swarup, and J. M. Thomas, "Dielectric properties of normal and malignant human breast tissues at radiowave and microwave frequencies," *Indian J. Biochem. and Biophys.*, vol. 21, pp. 76–79, Feb. 1984.

[5] S. C. Hagness, K. M. Leininger, J. H. Booske, and M. Okoniewski, "Dielectric characterization of human breast tissue at microwave frequencies," in Proc. 2nd World Congress on Microwave and Frequency Processing, Orlando, FL, Apr. 2000.

[6] S. C. Hagness, A. Taflove, and J. E. Bridges, "Two-dimensional FDTD analysis of a pulsed microwave confocal system for breast cancer detection: Fixed-focus and antenna-array sensors," *IEEE Trans. Biomed. Eng.*, vol. 45, no. 12, pp. 1470–1479, Dec. 1998.

[7] A. S. Swarup, S. S. Stuchly, and A. Surowiec, "Dielectric properties of mouse MCA1 fibrosarcoma at different stages of development," *Bioelectromagn.*, vol. 12, pp. 1–8, 1991.

[8] K. R. Foster and H. P. Schwan, "Dielectric properties of tissues and biological materials: A critical review," *Critical Rev. Biomed. Eng.*, vol. 17, pp. 25–104, 1989.

[9] A. E. Souvorov, A. E. Bulyshev, S. Y. Semenov, R. H. Svenson, and G. P. Tatsis, "Two-dimensional computer analysis of a microwave flat antenna array for breast cancer tomography," *IEEE Trans. Microwave Theory Tech.*, vol. 48, pp. 1413–1415, Aug. 2000.

[10] A. E. Bulyshev, S. Y. Semenov, A. E. Souvorov, R. H. Svenson, A. G. Nazarov, Y. E. Sizov, and G. P. Tatsis, "Computational modeling of three-dimensional microwave tomography of breast cancer," *IEEE Trans. Biomed. Eng.*, vol. 48, pp. 1053–1056, Sept. 2001.

[11] P. M. Meaney and K. D. Paulsen, "Nonactive antenna compensation for fixed-array microwave imaging: Part II-Imaging results," *IEEE Trans. Med. Imag.*, vol. 18, pp. 508–518, June 1999.

[12] P. M. Meaney, M. W. Fanning, D. Li, S. P. Poplack, and K. D. Paulsen, "A clinical prototype for active microwave imaging of the breast," *IEEE Trans. Microwave Theory Tech.*, vol. 48, pp. 1841–1853, Nov. 2000.

[13] Q. H. Liu, Z. Q. Zhang, T. T. Wang, J. A. Bryan, G. A. Ybarra, L. W. Nolte, and W. T. Joines, "Active microwave imaging I – 2-D forward and inverse scattering methods," *IEEE Trans. Microwave Theory Tech.*, vol. 50, pp. 123–133, Jan. 2002.

[14] S. Hagness, A. Taflove, and J. E. Bridges, "Three-dimensional FDTD analysis of a pulsed microwave confocal system for breast cancer detection: Design of an antenna-array element," *IEEE Trans. Antennas Propagat.*, vol. 47, pp. 783–791, May 1999.

[15] X. Li and S. C. Hagness, "A confocal microwave imaging algorithm for breast cancer detection," *IEEE Microwave Wireless Components Lett.*, vol. 11, pp. 130–132, Mar. 2001.

[16] E. C. Fear and M. A. Stuchly, "Microwave detection of breast cancer," *IEEE Trans. Microwave Theory Tech.*, vol. 48, pp. 1854–1863, Nov. 2000.

[17] W. H. Parsons, *Cancer of the Breast*. Springfield, IL: Charles Thomas, 1959.

[18] S. Haykin, *Adaptive Filter Theory*, 3rd ed. Upper Saddle River, NJ: Prentice-Hall, 1996.

[19] B. Van Veen, "Minimum variance beamforming," in *Adaptive Radar Detection and Estimation*, S. Haykin and A. Steinhardt, Eds. New York: Wiley, 1992, ch. 4, pp. 161–236.

[20] H. Cox, R. M. Zeskind, and M. M. Owen, "Robust adaptive beamforming," *IEEE Trans. Acoust., Speech, Signal Processing*, vol. ASSP-35, pp. 1365–1376, Oct. 1987.

[21] A. Taflove and S. Hagness, *Computational Electrodynamics: The Finite-Difference Time-Domain Method*, 2nd ed. Boston, MA: Artech House, 2000.

[22] R. M. Joseph, S. C. Hagness, and A. Taflove, "Direct time integration of Maxwell's equations in linear dispersive media with absorption for scattering and propagation of femtosecond electromagnetic pulses," *Optics Lett.*, vol. 16, no. 18, pp. 1412–1414, 1991.

Essex Bond (S'98) was born in Milwaukee, WI. He received the B.S. degree from the Milwaukee School of Engineering, in 1999 and the M.S. degree from the University of Wisconsin-Madison (UW), in August 2001, both in electrical engineering, where is currently working toward the Ph.D. degree in the Department of Electrical and Computer Engineering.

His research interests include statistical signal processing, biomedical applications of signal processing, adaptive filtering, and image reconstruction techniques.

Mr. Bond was the recipient of a Graduate Engineering Research Scholars Fellowship from the University of Wisconsin-Madison in 1998.

Xu Li (S'99) was born in Beijing, China. She received the B.S. degree in biomedical engineering from Tsinghua University, Beijing, China and the M.S. degree in biomedical engineering from the University of Wisconsin-Madison, in 1998 and 2000, respectively, where she is currently working toward the Ph.D. degree in the Department of Electrical and Computer Engineering.

Her research interests include microwave imaging techniques for breast cancer detection, FDTD computational electromagnetics modeling, signal processing and image reconstruction techniques, and ultra-wideband antennas.

Ms. Li was the recipient of a Wisconsin Alumni Research Foundation Graduate Fellowship from the University of Wisconsin-Madison in 1998.

Susan C. Hagness (S'91–M'98) received the B.S. degree with highest honors and the Ph.D. degree in electrical engineering from Northwestern University, Evanston, IL, in 1993 and 1998, respectively.

While at Northwestern University, she was the recipient of an NSF Graduate Fellowship and was named a Tau Beta Pi Spencer Fellow. Since August 1998, she has been with the University of Wisconsin-Madison, where she is currently an Assistant Professor in the Department of Electrical and Computer Engineering and a Faculty Affiliate of the Department of Biomedical Engineering. Her research interests include FDTD theory and applications, microwave imaging and sensing techniques for biological and medical applications, and full-wave analysis and design of photonic microstructures. She coauthored *Computational Electrodynamics: The Finite-Difference Time-Domain Method*, (Boston: Artech House, 2nd. ed., 2000) with A. Taflove.

Dr. Hagness received the Presidential Early Career Award for Scientists and Engineers from the White House in 2000. She also received the Holdridge Excellence in Teaching Award from the ECE Department at the University of Wisconsin. In 2002, she received the Booker Fellowship Award from the United States National Committee of URSI. She was also named one of the 100 Top Young Innovators in Science and Engineering in the world by MIT's *Technology Review magazine*. In 2003, she received the University of Wisconsin Emil Steiger Distinguished Teaching Award. She is currently serving as an Associate Editor for the IEEE ANTENNAS AND WIRELESS PROPAGATION LETTERS and as a Member of the IEEE Propagation Society Administrative Committee (AdCom).
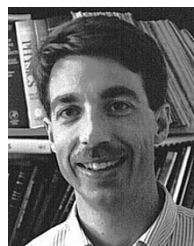
Barry D. Van Veen (S'81–M'86–SM'97–F'02) was born in Green Bay, WI. He received the B.S. degree from Michigan Technological University in 1983 and the Ph.D. degree from the University of Colorado in 1986, both in electrical engineering. He was an ONR Fellow while working on the Ph.D. degree.

In the spring of 1987 he was with the Department of Electrical and Computer Engineering at the University of Colorado-Boulder. Since August of 1987, he has been with the Department of Electrical and Computer Engineering at the University of Wisconsin-Madison, and currently holds the rank of Professor. He coauthored *Signals and Systems* (New York: Wiley, 1999). His research interests include signal processing for sensor arrays, nonlinear systems, adaptive filtering, wireless communications and biomedical applications of signal processing.

Dr. Van Veen was a recipient of a 1989 Presidential Young Investigator Award from the National Science Foundation, a 1990 IEEE Signal Processing Society Paper Award, and a Holdridge Teaching Excellence Award from the ECE Department at the University of Wisconsin in 1997. He served as an Associate Editor for the IEEE TRANSACTIONS ON SIGNAL PROCESSING and IEEE SIGNAL PROCESSING LETTERS. He was a Member of the Society's Technical Committee on Statistical Signal and Array Processing from 1991 through 1997 and is currently a Member of the Sensor Array and Multichannel Technical Committee.